Numerical investigation of the role of hyper-mixers in supersonic mixing

S. L. N. Desikan

Department of Aerospace Engineering, IIT Madras
Chennai, India

K. Kumaran

V. Babu
vbabu@iitm.ac.in
Department of Mechanical Engineering, IIT Madras
Chennai, India

ABSTRACT

In this numerical study, the role of hyper-mixers on supersonic mixing is investigated for six different strut configurations. To this end, 3D, compressible, turbulent, non-reacting flow calculations with air as the secondary injectant have been carried out. A qualitative comparison of the predictions with experimental results is made through Schlieren and Mie scattering images. A quantitative evaluation of the predictions is made by comparison with experimentally measured exit stagnation pressure, wall static pressure and the degree of unmixedness. Based on these results, three strut configurations have been selected for carrying out simulations with hydrogen as the injectant. Results from the hydrogen simulations are compared with the predictions using air and also across the strut configurations. The results clearly demonstrate that castellated strut configurations are very effective in enhancing mixing in such high speed flows.

1.0 INTRODUCTION

Hypersonic air-breathing engines are considered to be the most appropriate alternative device to rocket based propulsion systems in reusable space vehicles within the lower atmospheric regime. Supersonic combustion ramjet (scramjet) engine is the key enabling technology for such sustained hypersonic flights. In scramjet engines, since the residence time of the mixture is of the order of a millisecond (for flight Mach numbers from 6 to 8) owing to the short combustor length, generation of useful thrust over the vehicle drag through heat addition at such high speeds is a challenging task. This is due to the fact that the fuel has to mix and burn completely within the short combustor length. Consequently, this places a severe limitation on the mixing time scale. This emphasises the importance of fuel injectors and mixing enhancement devices in supersonic combustors.

Over the years, several fuel injection strategies such as, strut[1,2,3], wall[4] and several flame holding strategies such as, rearward facing step[5,6] and cavities of different configurations[7,8,9] have been proposed and extensively studied. In addition, mixing can also be enhanced using modified structures such as, ramps[10,11,12] and pylons[13,14]. The enhancement of mixing due to the stream-wise vortices introduced by modified structures has also been investigated[15,16,17]. However, strut based injection is reported to be the most promising strategy owing to the fact that the fuel can be injected at the middle of the combustor. In addition, the strut geometry bifurcates the main stream air and enhances the mixing of fuel injected from the strut with the main stream through the mixing of supersonic shear layers[18,19]. Recently, mixing enhancement has been attempted by using modified structures in conjunction with the strut, which are classified as hyper-mixers, in hypersonic flows[12,15]. Although hyper-mixers are reported to show promise for the enhancement of mixing in model combustors, the extendibility of this concept to full scale combustors still warrants further investigation, owing to the fact that the loss associated with the hyper-mixers can be high.

In this work, the role of hyper-mixers on the enhancement of the mixing of fuel and air in a supersonic cross-flow is investigated. Several novel configurations have been designed, modeled and experimentally tested in an earlier investigation[20]. Owing to facility constraints, air, rather than an actual fuel, was used as the injectant in the experiments. Numerical simulations with air as the injectant have been carried out for selected configurations and the predictions are validated with the experimental results. Following this, results from simulations using an actual fuel such as hydrogen as the secondary injectant, are presented and the role of the hyper-mixers on the mixing performance is highlighted.
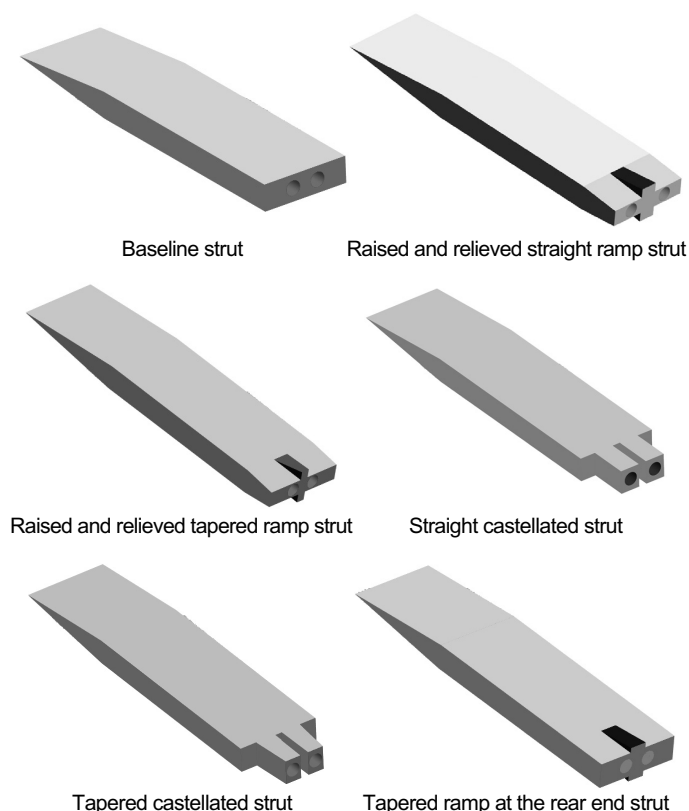
2.0 COMPUTATIONAL METHODOLOGY

The strut geometries considered here are shown in Fig. 1. The test section is a rectangular constant area duct of length 300mm, height 80mm and width 20mm with the strut located in the middle. Six strut configurations have been identified from the experimental work[20] for the numerical investigation. Pure air (with the mass fractions of O_2 and N_2 being 0·23 and 0·77 respectively) enters the facility nozzle. The flow is accelerated to a nominal Mach number of 1·7 as it enters the test section. The flow in the divergent part of the nozzle has also been simulated to capture the boundary layer on the walls accurately and to match the experimental test section inlet conditions. Air (or hydrogen) is injected from two circular injectors located on the strut base. Since all the simulations have been performed on quarter geometry based on symmetry consideration, the fuel is injected only from a quarter injection port (Fig. 2). In the simulations, three dimensional, compressible and turbulent Favre-averaged Navier Stokes equations are solved. All the simulations have been carried out using FLUENT.

Turbulence has been modeled using the two equation, SST k-ω turbulence model[21]. The SST k-ω model is a hybrid of the standard k-ε and k-ω models. This model is essentially a standard k-ω model near solid surfaces, which gradually switches to the standard high Reynolds number k-ε model away from solid surfaces. This feature combines the near-wall robustness of the standard k-ω turbulence model with the capabilities of the k-ε model away from the walls. It also includes the effect of turbulent shear stress transport based on Bradshaw's[22] assumption, that the shear stress in a boundary layer is proportional to the turbulent kinetic energy. This modification improves the ability of this model to predict the flow separation better than the k-ε model. This model with default closure coefficients has been used in this study. The turbulent Schmidt number and Prandtl number are

Figure 1. Strut geometries with modifications near the trailing edge.

Table 1
Flow conditions at the test section inlet and secondary inlet

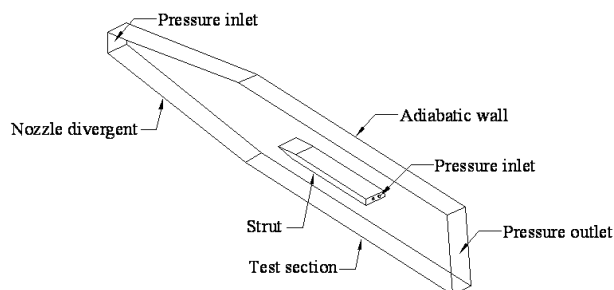|	
Main Fluid	N_2 and O_2 (0·77, 0·23)
Mach number	1·7
Total pressure	5 bar (abs)
Total temperature	300K
Mass flow rate	1·38kg/s
Secondary fluid	Air or Hydrogen
Mach number	1 (Sonic)
Total pressure	5 bar(abs)
Total temperature	300K
Mass flow rate	0·02kg/s (air) or 0·0056kg/s (hydrogen)

Figure 2. Computational domain.

taken to be equal to 0·7 and 0·667 respectively. Sensitivity of the numerical predictions to the turbulent Schmidt number has already been investigated for ethylene[23] and hydrogen[24] fuel.

Viscosity and C_p of the mixture have been evaluated using a mass-weighted-mixing law. For the individual fluids in the mixture these properties have been specified as constants, since the temperature range is not large in the non-reacting flow calculations.

2.1 Boundary conditions

At the nozzle throat, where the flow enters at sonic condition, the total pressure, total temperature and species mass fractions are specified (Table 1). For the secondary injection, air or hydrogen is injected from the strut base at sonic condition. This is modelled as a pressure inlet where the total pressure, total temperature and the species mass fractions are specified. Although the injectant is air, this has been modeled as a different fluid to enable tracking of the secondary stream. At the test section outlet, where the flow is supersonic, all the flow properties are extrapolated from the interior of the domain. All the solid surfaces are stationary and adiabatic and standard wall functions have been used.

2.2 Convergence metrics

All the calculations are carried out until the global (overall) mass, momentum and energy balance is acceptable. For all the results reported here, the difference in overall mass flow rate between the inlet(s) and the outlet is less than 3% of the secondary injection mass flow rate (secondary injection mass flow rate rather than the test section inlet mass flow rate is used since the former is almost two orders of magnitude less than the latter). Momentum balance is also checked by evaluating the left and right hand sides of the expression

$$F = \left[\int \left(P + \rho u^2 \right) \mathrm{d}A \right]_{inlet}^{Outlet}$$

separately and then calculating the difference. The right hand side of this expression is the impulse function. The left hand side is the net force acting on the walls (pressure+ viscous) in the *x*-direction. For all the results reported here, the difference between the left and right hand side of the above expression is
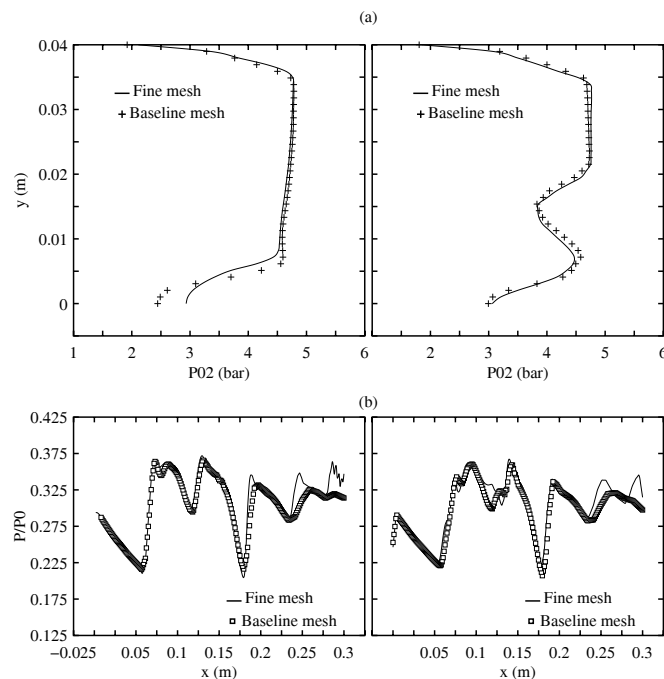

Figure 3. Comparison of the predictions obtained using the baseline mesh and fine mesh for the baseline geometry (left) and RRTR (right). (a) Exit P_{02} and (b) Non-dimensional static pressure on the top wall.

Table 2
Grid related details for the various geometries

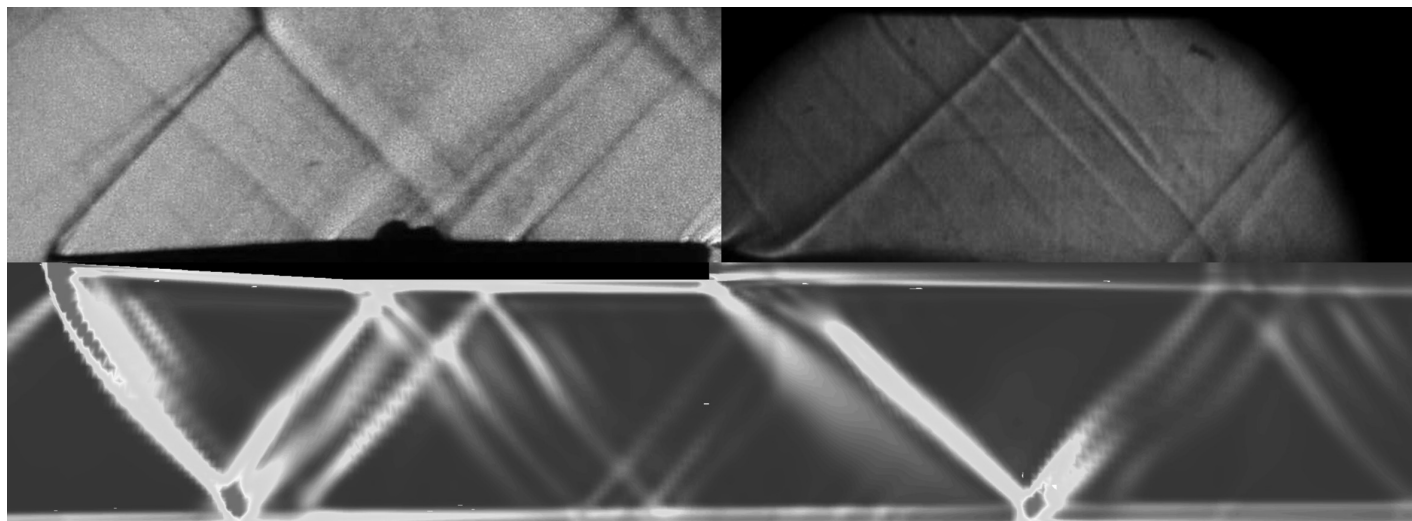| Geometry	No. of cells	Average wall y+
Baseline	412,343	29
	686,164	14
RRSR	412,850	22
RRTR	419,904	23
	740,690	13
SCS	427,975	27
TCS	416,555	26
TRRE	425,244	24

Figure 4. Comparison of the predicted (bottom) flow features with the experimental data (top) for the baseline strut.

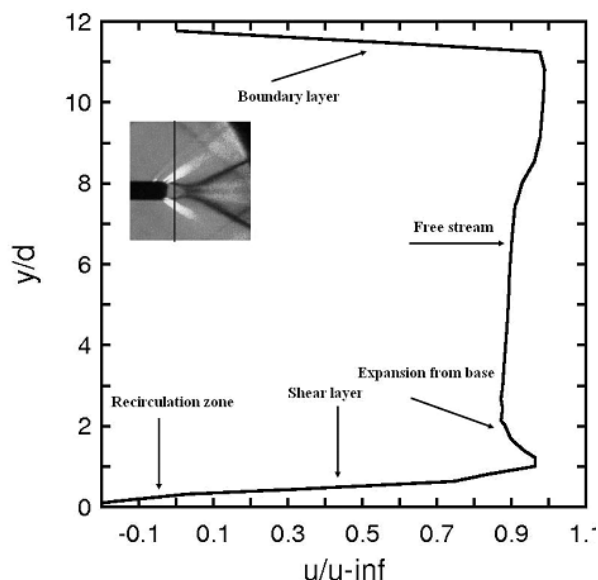Figure 5. Computed centerline velocity profile
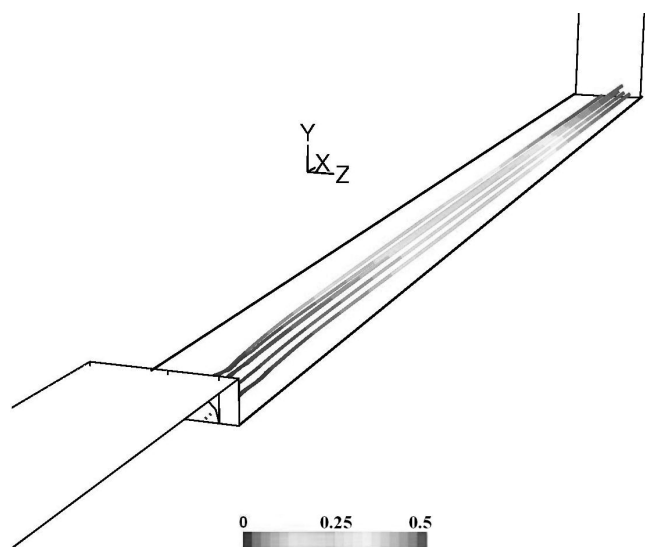at *x* = 100mm for the baseline case.

Figure 6. Pathlines of the secondary injectant coloured with the time of
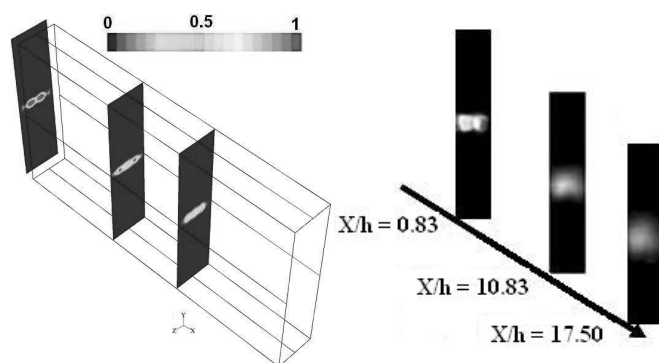flight (in milliseconds) for the baseline strut configuration.

Figure 7. Contours of mole fractions of the secondary injectant
for the baseline strut: Numerical (left) and experiment (right).

2.3 Grid independence study

A structured grid has been used for meshing the entire geometry. Since the mainstream static temperature and in turn the kinematic viscosity are very low, the near wall mesh spacing had to be very small in order to achieve acceptable values for the wall y+ (it may be recalled that the wall y^+ is equal to $y_{wall} u_\tau/v$, where y_{wall} is the cell spacing near the wall, v is the kinematic viscosity of the fluid and $u_\tau = (\tau_{wall}/\rho)^{\frac{1}{2}}$ is the friction velocity.). The number of cells and the area weighted average of wall y^+ in the test section including the strut surface for the different geometries are given in Table 2. It is clear that the near wall cell lies in the log-law region of the boundary layer which justifies the use of the standard wall functions. Although there are geometrical differences at the rear end of the strut between the different strut configurations, considerable effort has been devoted to ensure that the total cell count in all the cases is more or less the same. This has been carried out without altering the boundarylayer resolution near the walls. Of course, it is important to resolve the flow features in the interior of the computational domain also. With this in mind, the mesh spacing in the interior is also kept fine, as otherwise the cells will become highly skewed. The maximum volume weighted average of cell equi-angle skew is 0·0364† in the entire domain.

Grid independence of the predictions has been investigated for two geometries, namely, baseline and raised and relieved tapered ramp strut. The baseline mesh for these geometries was refined, both near the walls and in the interior till the wall y^+ was halved (Table 2). The predictions obtained using these grids are shown in Fig. 3, where the static pressure on the top wall of the test section and the stagnation pressure (as measured by a pitot probe) at the exit are compared. The predictions are grid independent except near the corner at the exit, where the predictions show some difference, which can be attributed to the flow unsteadiness in this region that was noticed during the simulations.

3.0 RESULTS AND DISCUSSION

In this section, results from the numerical simulations of six strut configurations are presented and discussed. Contours of density gradient from the numerical simulations are compared with experimental Schlieren images. The trajectories of the secondary injection coloured with the time of flight are used to gain insights into the mixing process. In these comparisons, a common colour bar scale is used for all the cases in order to facilitate the visual comparison. Numerically predicted pressure distribution on the top wall and the total pressure at the test section exit are also compared with experimental data.

3.1 Air injection

3.1.1 Flow features

A Baseline strut (BS)

Figure 4 shows the comparison of experimental Schlieren flow field with the predicted density derivative for the baseline strut configuration. The numerical simulation is able to predict the leading-edge shock well. The point of impingement of the leading-edge shock on the test section wall and the resultant Mach reflection and the expansion fans have also been predicted well.

Downstream of the strut, there is a slight axial shift in the location of the point of impingement of the re-attachment shocks in the numerical predictions. However, the shock angle in the simulation is almost the same as seen in the experiment. This discrepancy could be due to unequal secondary injection mass

† An equi-angle skew measure of 0 indicates a perfect hexahedron and a value of 1 denotes a degenerate one. In practice, skewness measure values below 0·6 are usually acceptable.
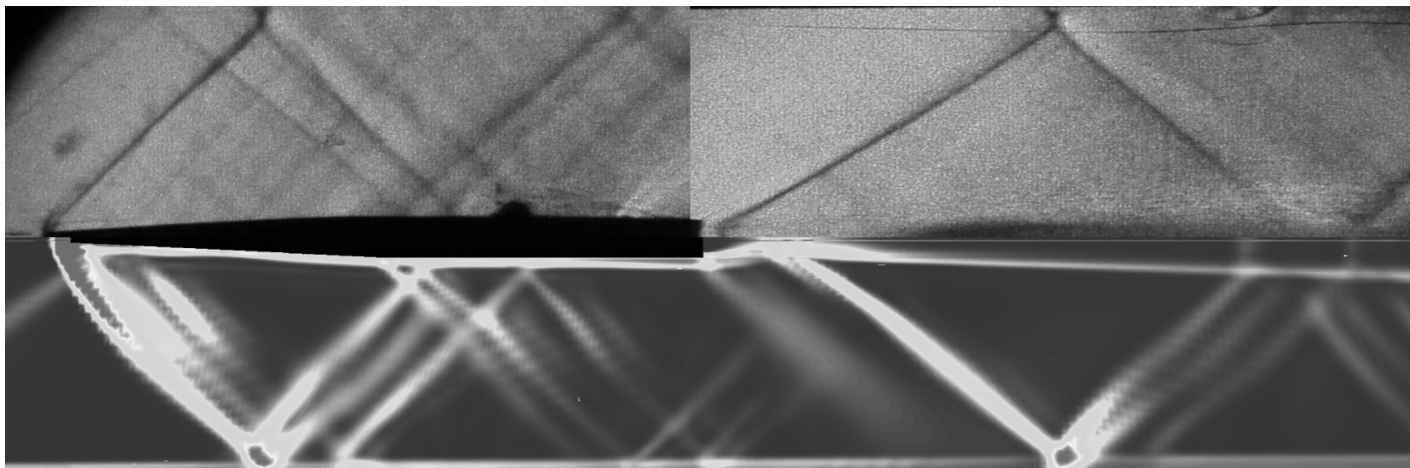
Figure 8. Comparison of the predicted (bottom) flow features with the experimental data (top) for the straight castellated strut.

flow rates in the experiment. In the experiments, the secondary air is supplied to the two injection ports from the test section side wall on either side of the strut. Although the total pressure is the same on both the sides, there is a possibility of a slight mismatch in the mass flow rates through the two injection ports.

The subsonic re-circulation zone in the base region of the strut and the outer supersonic flow are separated by a shear layer. The characteristic of the shear layer is the uniform change of super-sonic outer flow to subsonic flow inside the re-circulation zone. This can be seen from the computed axial velocity profile at $x = $ 100mm downstream of the strut leading-edge as shown in Fig. 5. Here, the computed velocity profile and the y-co-ordinate are made non-dimensional with the inlet velocity and injector diameter (3·4mm) respectively. The salient features in the velocity profile are marked in the figure. The negative velocity near $y = 0$ indicates the existence of a re-circulation region. The shear layer is discernable for $0·2 \leq y/d \leq 1·7$. The increase in the axial velocity above the value corresponding to the core super-sonic flow ('free stream') is due to the expansion fan emanating from the corner of the base region.

Figure 6 shows the trajectories of the secondary jet coloured with time of flight for the baseline strut configuration. Here, the pathlines of the secondary jet initially converge in the y-direction and then diverge further downstream. This is consistent with the Schlieren image shown in Fig. 4. Pathlines clearly show that the spread of the secondary fluid is minimal in the lateral as well as in the vertical directions along the entire test section.

Figure 7 shows the comparison of mole fraction contours of the secondary injection at three axial locations namely $X/h = 0·83$, 10·83 and 17·5 along the test section, where, X is the axial distance along the test section length and h is the height of the strut. The predicted mole fraction contours show good agreement with the trends in experimental data obtained using Mie-scattering technique. At $X/h = 0·83$, the core region is clearly visible in both cases. The spread of the secondary injectant is uniform across the test section and starts from the periphery of the jet. However, the rate of spread is seen to be gradual. This highlights the fact that although a strut is used to inject in the middle of the domain along the flow direction, the influence of the strut on the spreading or mixing of the secondary fluid with the mainstream is marginal. These results clearly highlight the need for additional devices to enhance the mixing. These are discussed next.

B Straight castellated strut (SCS)

Figure 8 shows the comparison of predicted flow features with the experimental findings for the straight castellated strut. Here, there
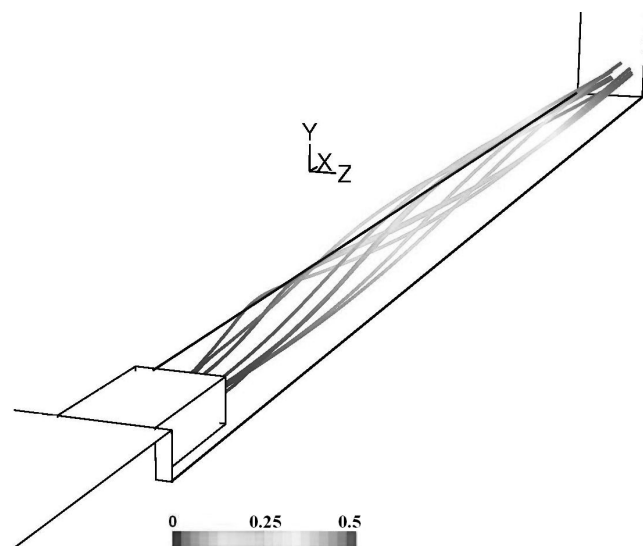

Figure 9. Pathlines of the secondary injectant coloured with the time of flight (in milliseconds) for the straight castellated strut configuration.
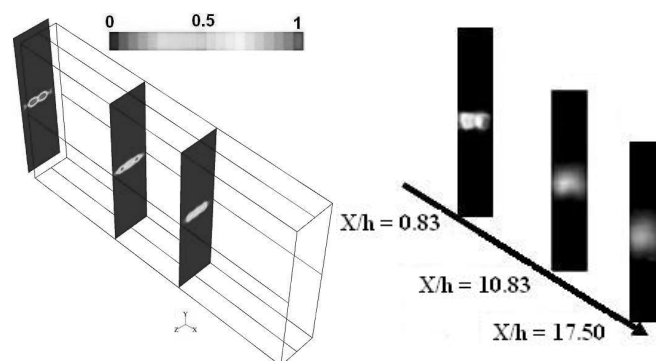

Figure 10. Contours of mole fractions of the secondary injectant for the straight castellated strut: Numerical (left) and experiment (right).
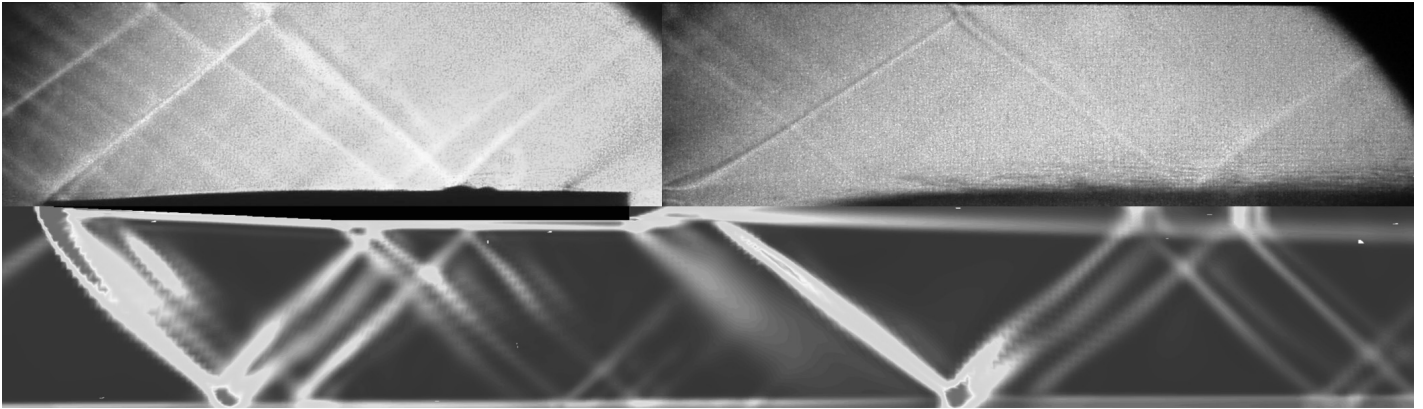
Figure 11. Comparison of the predicted (bottom) flow features with the experimental data (top) for the tapered castellated strut.
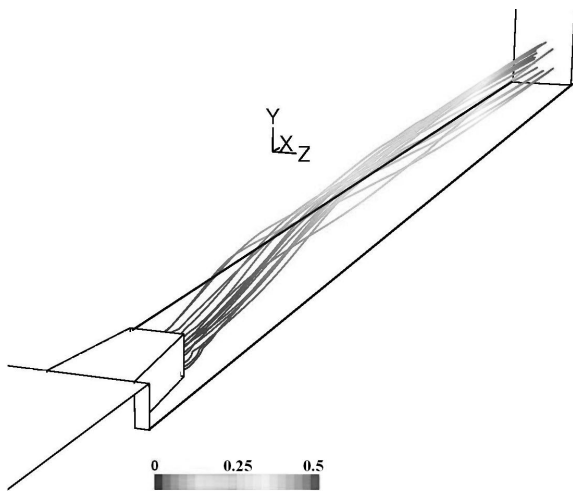

Figure 12. Pathlines of the secondary injectant coloured with the time of flight (in milliseconds) for the tapered castellated strut.
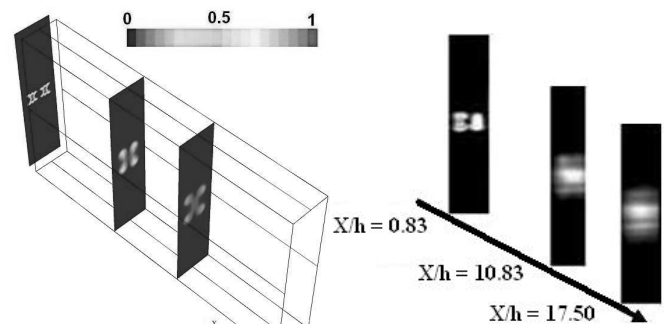

Figure 13. Contours of mole fractions of the secondary injectant for the tapered castellated strut: Numerical (left) and experiment (right).

is a slight mismatch between the predicted leading-edge shock angle and the experimental data. Consequently, this results in a shift in the point of impingement of the leading-edge shock on the test section walls thereafter. This can be due to a small offset in the positioning of the strut in the experiment and in supersonic flows even such a small offset can lead to a completely different flow pattern. However, the expansion fans generated in the recess region and the oblique shock from the wake region behind the strut are captured well by the simulations.

Figure 9 shows the pathlines of the secondary injection for the straight castellated strut. The initial necking and the subsequent expansion of the pathlines can be clearly seen in Fig. 8. The effect of the castellated geometry on the flow and pathlines are evident from the interweaving pattern of the trajectories along the test section length. From the colour of the pathlines, it can be surmised that the residence time is longer now than in the baseline case.

Figure 10 shows the predicted mole fraction contours and experimental observations at three locations along the test section length. The trends in the predicted mole fraction contours agree very well with the experimental data. At the initial location, two secondary injection plumes are distinctly seen in the experiments and the simulation. As the plumes move downstream, spreading and mixing takes place both in the spanwise and vertical direction. The distortion of the plumes in the spanwise and vertical direction could be caused by the vortices generated from the projected and recessed parts of the strut. In this case, the rate of spread is rapid and uniform. This is consistent with the pathlines in Fig. 9.

C. Tapered Castellated Strut (TCS)

The comparison of flow field predictions with the experimental Schlieren image for the tapered castellated strut is shown in Fig. 11. A weak oblique shock emanating from the test section inlet is seen to impinge on the strut nose. The interaction between this shock and the leading-edge shock results in multiple shock reflections from the wall. This is not seen in the experiments. In addition, there is an offset in the point of interaction of the leading-edge shock on the wall in the simulations when compared with experimental findings. This offset prevails in other locations such as reflection from the wall, reattachment shock and its reflection from the wall. From Fig. 11, it is evident that the shock angles of the leading-edge shock and the re-attachment shocks are somewhat higher in the numerical predictions when compared with the corresponding values in the experiment.

Pathlines for the tapered castellated strut in Fig. 12 are seen to be very different from the straight castellated strut configuration shown in Fig. 9. In this case, a significant lifting of the pathlines in the vertical direction and a considerable deflection in the spanwise direction are seen. This brings out the fact that a small taper in the castellation can alter the flow field significantly and in turn the spreading and mixing of the secondary injectant. These changes in the secondary injectant flow pattern can be expected to cause an additional time delay in the time of flight and in turn an increase in the residence time when compared to the earlier cases. This also shows that the lateral spread of the secondary jet can be increased by using a tapered castellation. Since the flow field is entirely different from the earlier one, the
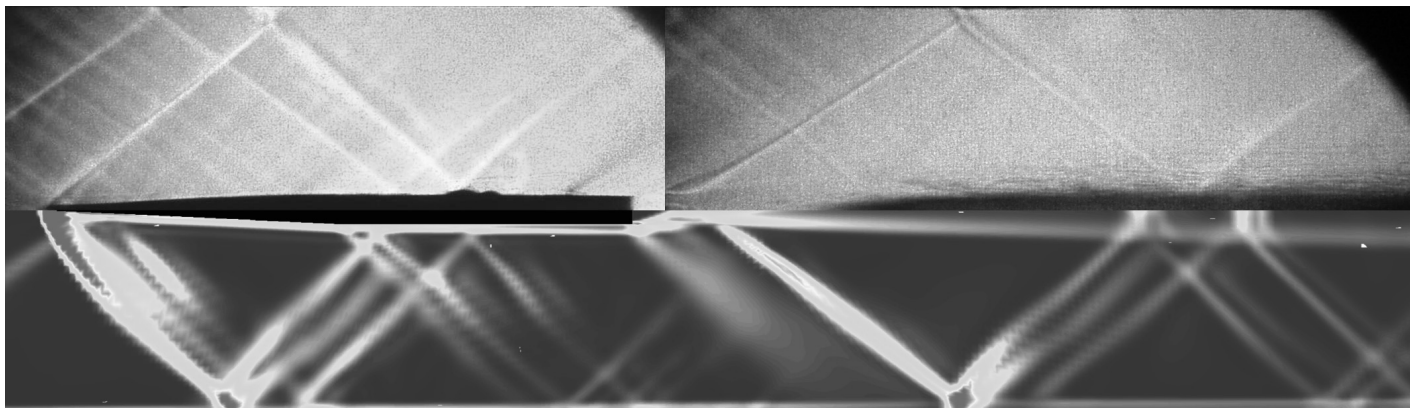
Figure 14. Comparison of the predicted (bottom) flow features with the experimental data (top) for the raised and relieved straight ramp strut.
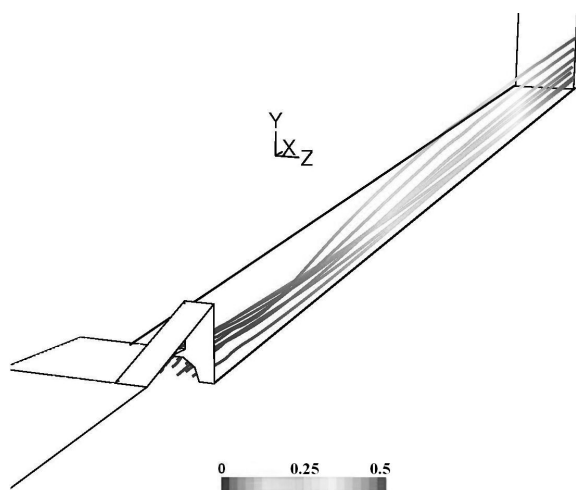

Figure 15. Pathlines of the secondary injectant coloured with the time of flight (in milliseconds) for the raised and relieved straight ramp strut.
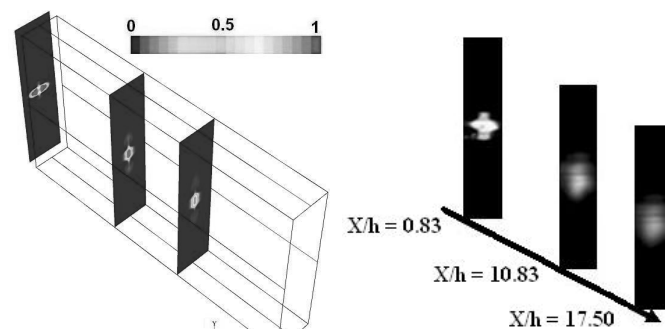

Figure 16. Contours of mole fractions of the secondary injectant for the raised and relieved straight ramp: Numerical (left) and experiment (right).

strengths of the vortices generated from the extended structures are likely to be different. This is discussed next using the distribution of the injectant mole fraction contours shown in Fig. 13.

At an axial location close to the strut rear end, both the simulation and experiment show a distinct core region of the secondary injection. As the secondary jets move down stream, they spread in both spanwise and vertical directions. This spread is clearly seen in the numerical results but not in the experimental images owing to hardware limitations. Although uniform mixing takes place in both the cases, the spread is predicted to be faster when compared to the experimental data. This can be seen by comparing the mole fraction contours at $X/h = 17\cdot50$ between numerical and experimental images, where the core region is still present in the latter case.

D Raised and Relieved Straight Ramp (RRSR) Strut

The leading-edge shock intersection points, re-attachment shock origin and its intersection point, wall reflection points are reproduced almost faithfully in the numerical simulation as seen in Fig. 14.

However, multiple reflections of shocks from the wall near the leading-edge are seen due to the interaction between the leading-edge shock and the shock emanating from the test section inlet, which is not present in the experiment. The ramp generated shocks are not strong enough to get reflected from the wall. The expansion fans from the relieving corner of the ramp are also predicted well. The boundary of the secondary jet spread is seen both in the experiment and numerical simulation.

Since there is no recess region near the side walls at the strut rear end (as seen in Figs 9 and 12), the pathlines of the secondary injectant shown in Fig. 15 are very similar to those seen in the baseline case. Hence the lateral spread of the secondary injectant is almost nil. However, due to the presence of the raised ramp the secondary jet is distorted in the vertical direction along the entire test section. The trends observed in the pathlines in this case are interesting since this case has the maximum spread in the vertical direction when compared to all the earlier cases, due to the generation of streamwise vortices by the raised ramp. Although the vertical spread seems to be better in this case, the residence time is almost the same as that of the baseline case. This indicates that the mixing may not be very effective.

The above observations are further supplemented by the mole fraction contours of the secondary injectant in Fig. 16. This clearly shows that there is a considerable distortion of the secondary jet in the vertical direction when compared to the lateral direction. The overall mixing or the rate of spread is predicted to be gradual when compared to the experimental results. Immediately downstream of the strut, the numerical simulation could not capture the two circular lobes above and below the elliptical injectant plume seen in the experimental Mie scattering images. The reason for this is not known.

The above results emphasise the fact that the lateral spread can be increased by a taper (as seen in Fig. 12) and the vertical spread can be enhanced by using a ramp (as seen in Fig. 15). This in turn suggests that a raised and relieved tapered ramp strut may lead to enhanced mixing. This is investigated next.
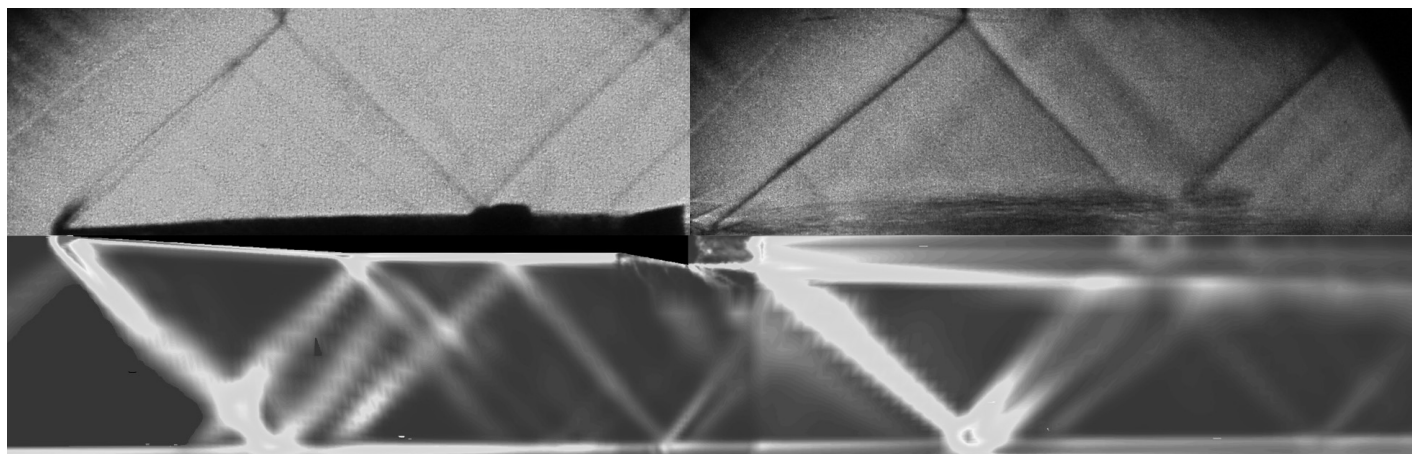
Figure 17. Comparison of the predicted (bottom) flow features with the experimental data (top) for the raised and relieved tapered ramp strut.
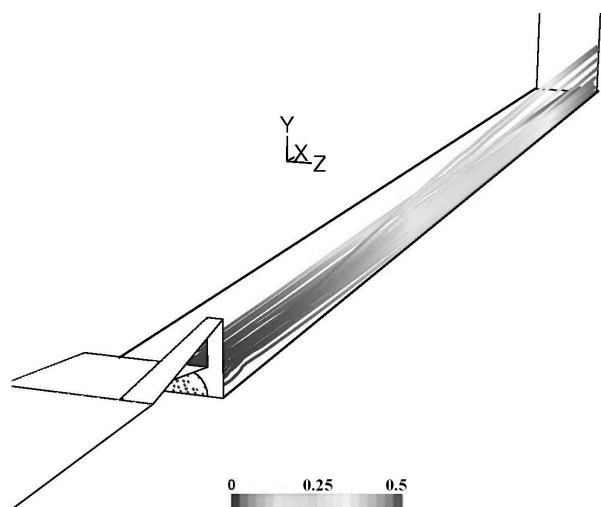

Figure 18. Pathlines of the secondary injectant coloured with the time of flight (in milliseconds) for the raised and relieved tapered ramp strut.
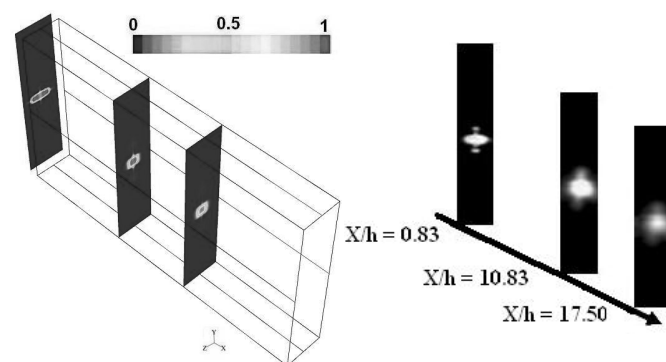

Figure 19. Contours of mole fractions of the secondary injectant for the raised and relieved tapered ramp strut: Numerical (left) and experiment (right).

E. Raised and Relieved Tapered Ramp (RRTR) Strut

Figure 17 shows the comparison of the predicted flow field with the experimental observation. Except for a few marginal differences, the predicted flow field agrees quite well with the experimental data. Since it is difficult to quantify the levels of the gradient from the experimental images, exact comparison of the numerical results with the experimental data is not possible. These images show that the predictions are able to capture the main flow features to a reasonable extent.

As expected, this configuration is able to produce a significant spread in the lateral as well as in the vertical direction as shown in Fig. 18. As mentioned earlier, the presence of a taper and a ramp can result in a considerable lateral and vertical spreading in the secondary jet respectively. Since, there is both lateral and vertical spreading the residence time can be expected to be longer and the mixing, in turn, better.

The trends predicted in the mole fraction contours shown in Fig. 19 agree quite well with the Mie scattering images from the experiment. The overall spreading across the cross section and the rate of spread is seen to be better in this case. However, the spreading is still seen to be inferior when compared to the castellated struts.

F. Tapered ramp at rear end (TRRE) strut

The tapered ramp at the rear end without any relief is investigated to bring out the effect of the ramp alone on mixing. Predicted and experimentally visualised flow fields for this geometry are shown in Fig. 20. Although the ramp generated shocks are visible, the strength of the shock is not sufficient enough to reflect back from the walls and intersect the secondary jet. The impingement location of the leading-edge shock is well captured in the simulation. However, as before, there is an offset in the location of the re-attachment shock and the angle at which the re-attachment shock is incident on the wall. This discrepancy can be attributed to a slight geometrical mismatch at the junction of the nozzle exit and the test section inlet. It is also clear that the expansion of the secondary jet is only marginal when compared to Fig. 17.

Figure 21 shows the pathlines of the secondary jets for the tapered ramp at rear end geometry. Although the ramp is present at the rear end of the strut, the spreading of the secondary stream in the vertical direction is seen to be minimal. In addition, a unique trend is observed with this configuration, in that the pathlines converge towards the center of the test section, which was not seen in the earlier cases. The reason for this trend in this configuration is not clear.

Predicted trends in the injectant mole fraction on planes immediately downstream of the strut agree well with those seen in the experiments (Fig. 22). However, the predicted spread of the secondary jet is seen to be gradual till $X/h = 17·50$ in contrast to the experimental finding. Since it is not possible to process the images from the numerical results in the exact same manner as the experimental images, it is difficult to make a one to one comparison between the two.
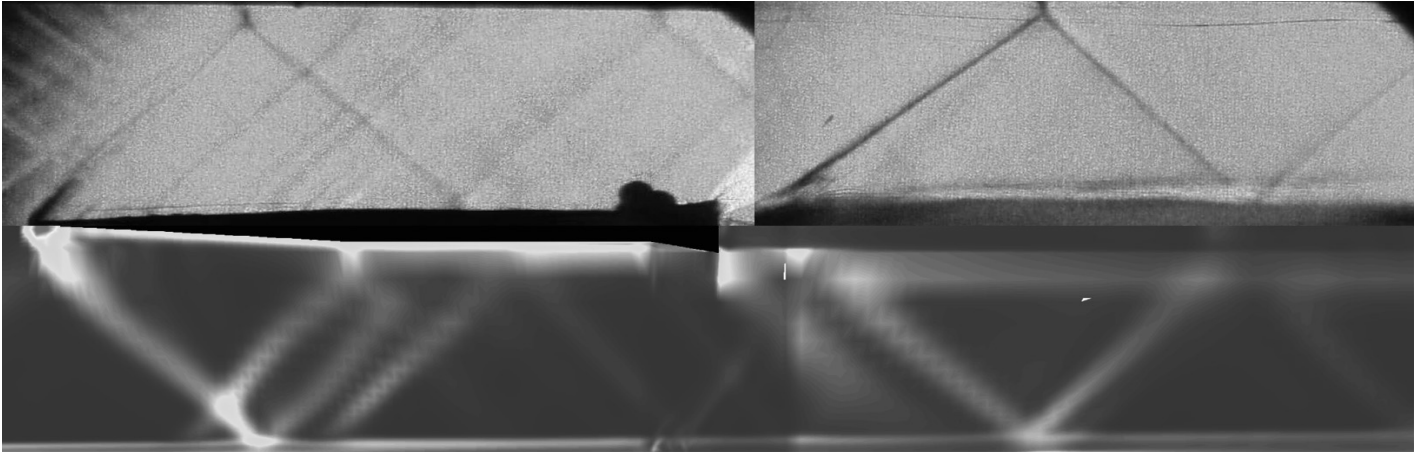
Figure 20. Comparison of the predicted (bottom) flow features with the experimental data (top) for the tapered ramp at rear end.
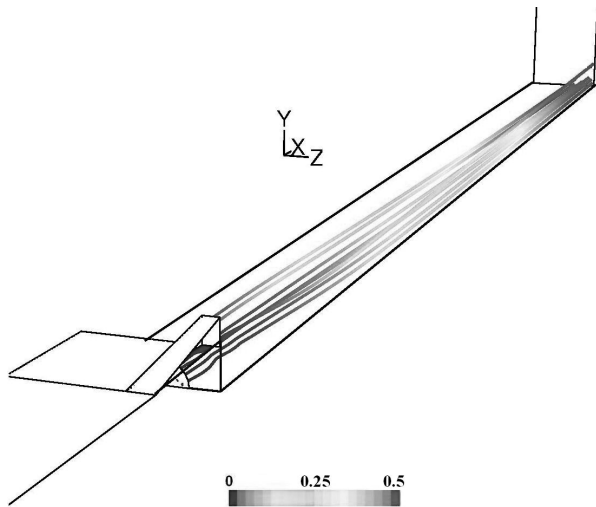

Figure 21. Pathlines of the secondary injectant coloured with the time of flight (in milliseconds) for the tapered ramp at rear end.

Figure 22. Contours of mole fractions of the secondary injectant for the tapered ramp at rear end strut: Numerical (left) and experiment (right).

3.1.2 Comparison of the exit stagnation pressure profile

Figure 23 shows the comparison of the stagnation pressure along the vertical centerline of the test section exit measured using a Pitot probe[20] and the predictions for all the six strut configurations. The numerical predictions plotted in this figure have been obtained from the calculated exit Mach number and stagnation pressure using the normal shock relation. The vertical height to which the injectant has penetrated can be clearly seen from this figure. The baseline case exhibits the penetration to be less than 12-15% of the test section height at the exit, whereas it is about 25% for the castellated configurations. The ramp configurations show even higher penetration. In all the cases, the predictions are within 10% of the experimental data except near the symmetry plane for the TRRE configuration. In this case, the difference is about 25% and it is clear that the mixing is not being predicted well. As mentioned earlier, the simulations exhibited varying degrees of unsteadiness close to the exit plane and this could be a reason for this discrepancy.

The raised and relieved straight and tapered ramps show a higher level of mixing around $y = 0.03$m. This kink in the exit total pressure curve can be traced to the fact that the oblique shock generated from the strut base is stronger in these two cases when compared to the other cases (Figs 14 and 17).
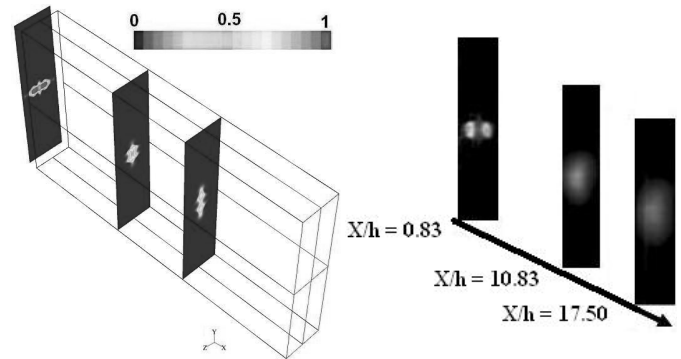
3.1.3 Comparison of the degree of unmixedness

In addition to the exit stagnation pressure profile, the degree of unmixedness has been used to quantitatively assess the performance of different strut configurations. Here, the degree of unmixedness from the predictions has been determined using a similar procedure followed in the experiments. The image of the contours of mole fraction of the injectant on an x constant plane is extracted and the degree of unmixedness (DU) at this axial location is calculated as

$$DU = \frac{1}{I_{avg}} \sum (I - I_{avg})^2 / N$$

where N is the number of pixels in the image, I is the intensity of a pixel and $I_{avg} = \frac{1}{N} \sum I$ is the average pixel intensity.

Figure 24 clearly shows that predictions are able to capture the trends seen in experiments. In all the cases, predictions are higher by about 8-10% than experimental values at all the axial locations downstream of the strut base. In the baseline case, since the mixing levels are low, the decrease in the degree of unmixedness is gradual and minimum. While, in the castellated strut configurations, the decrease is steep owing to high mixing levels from the strut base up to $x/h = 8$. This is due to the generation of vortices arising from the strut modifications. In this region, pathlines of the secondary injectant show the maximum dispersion across the cross section (as seen in
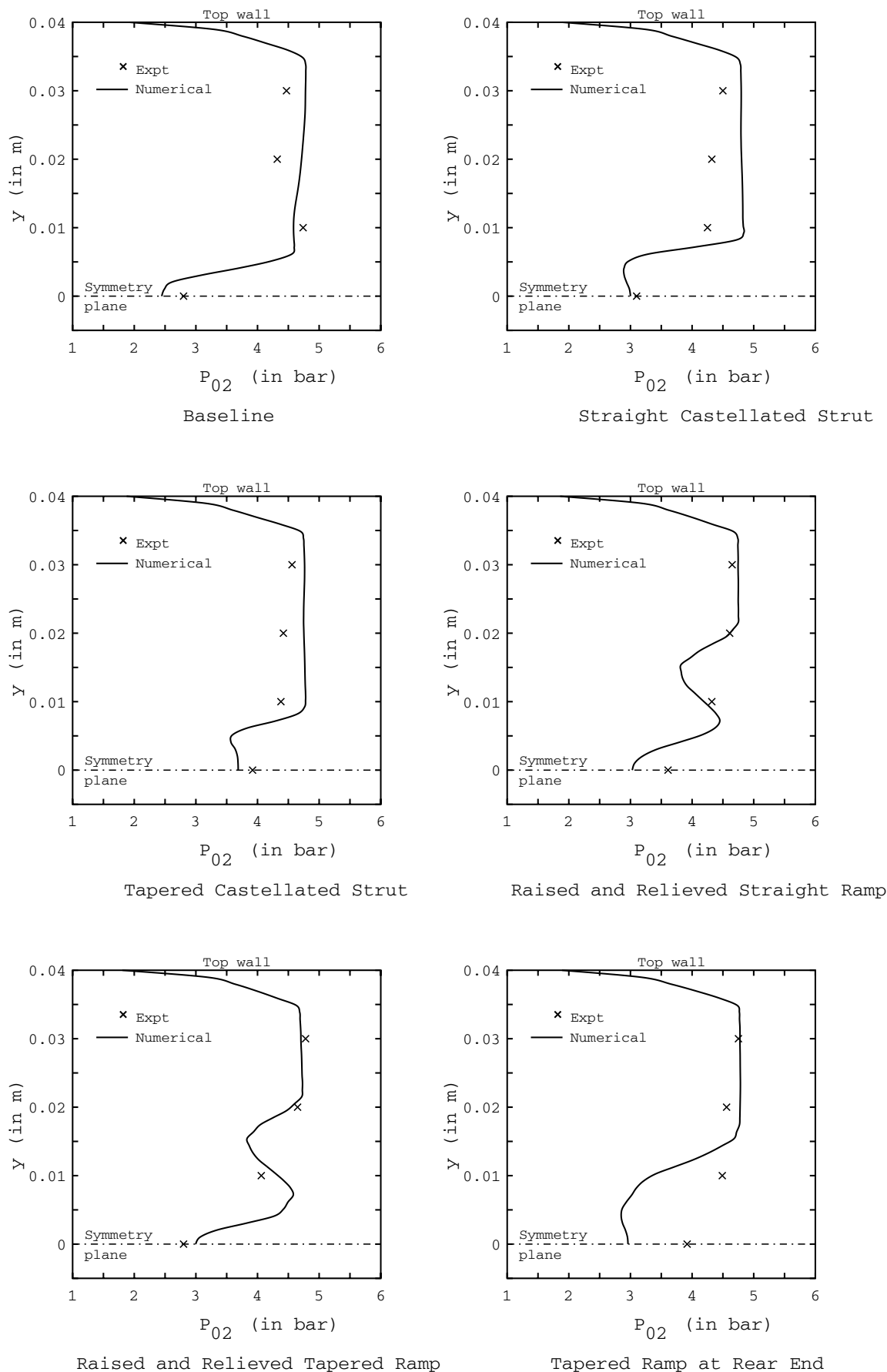
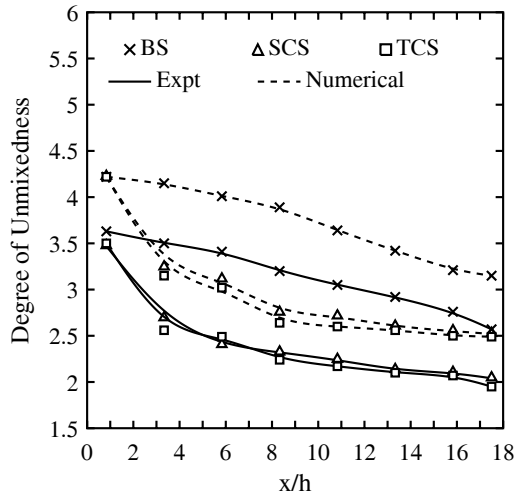Figure 23. Stagnation pressure profile at the test section exit.

Figure 24. Comparison of the degree of unmixedness for the baseline and straight and tapered castellated strut configurations.
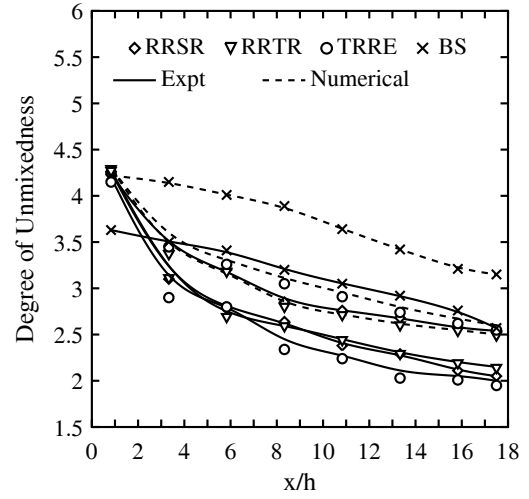
Figure 25. Comparison of the degree of unmixedness for tapered ramp at rear end (TRRE), raised and relieved, straight ramp (RRSR) and tapered ramp (RRTR) strut configurations.
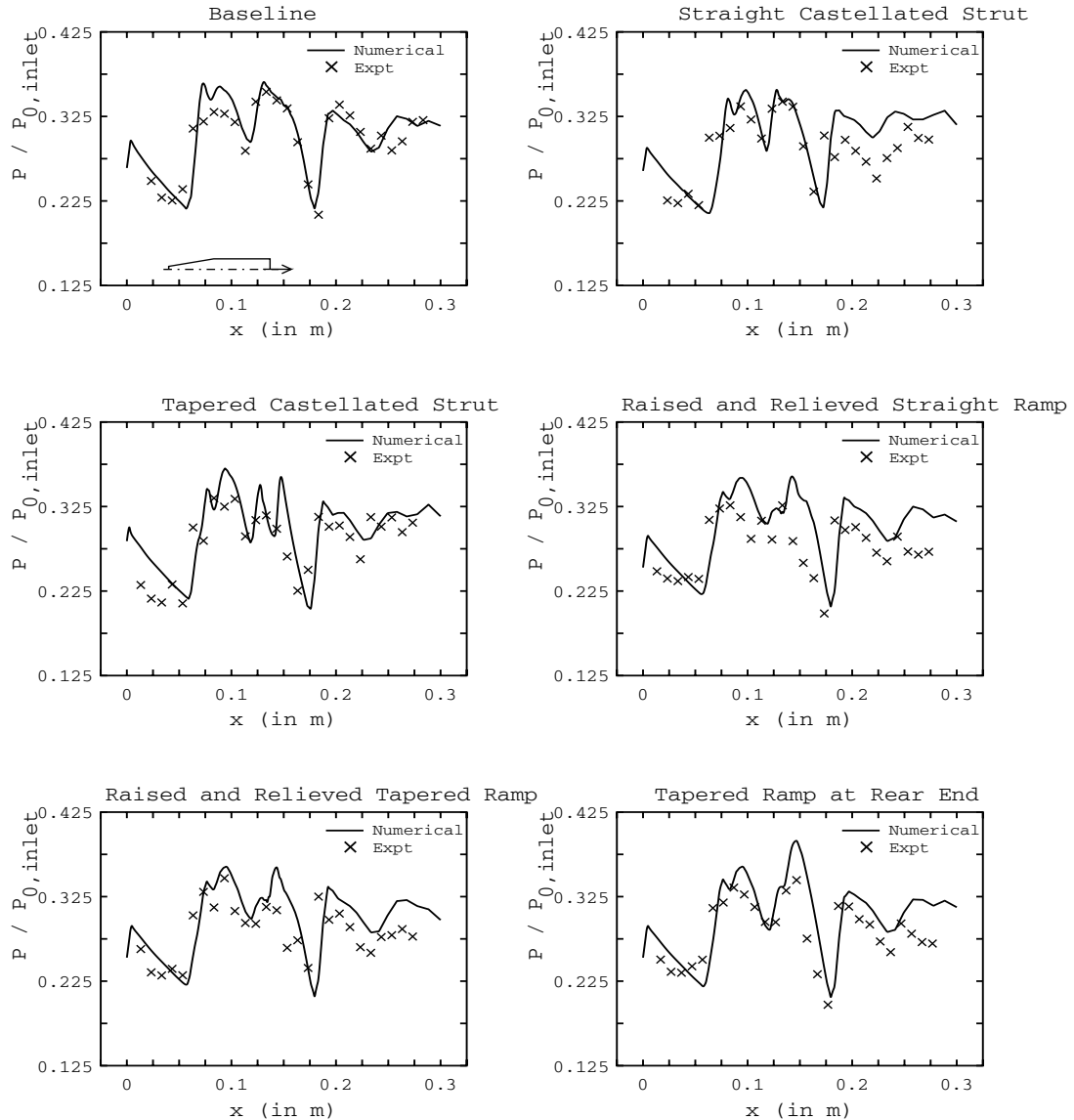
Figure 26. Comparison of the predicted wall static pressure with experimental data[25].
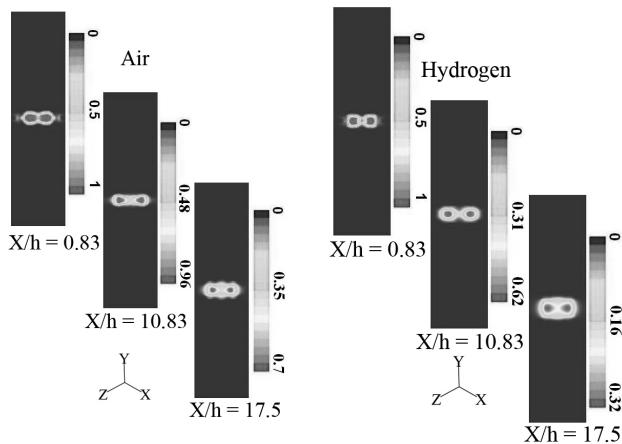
Figure 27. Contours of mass fractions of the
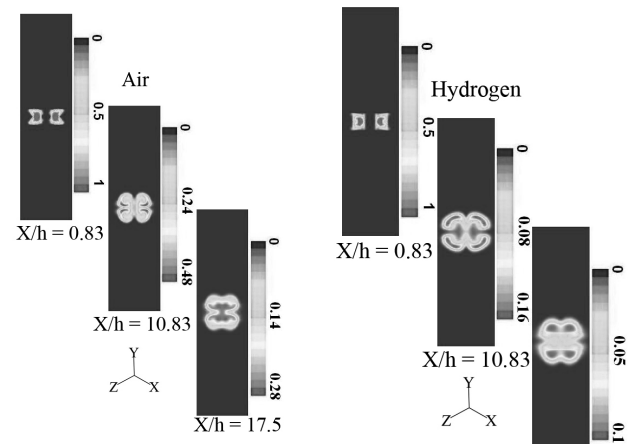injectant for the baseline strut configuration.

Figure 28. Contours of mass fractions of the injectants
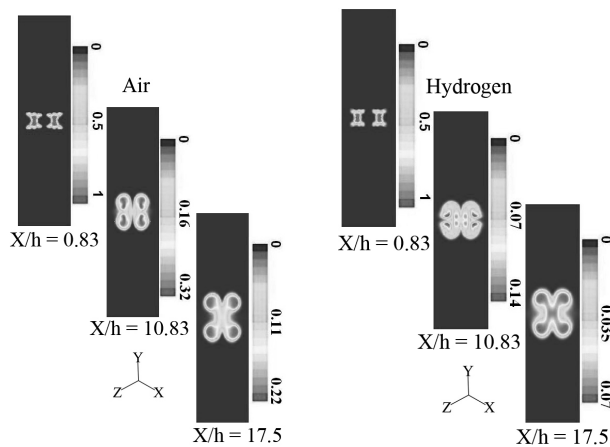for the straight castellated strut configuration.

Figure 29. Contours of mass fractions of the injectants
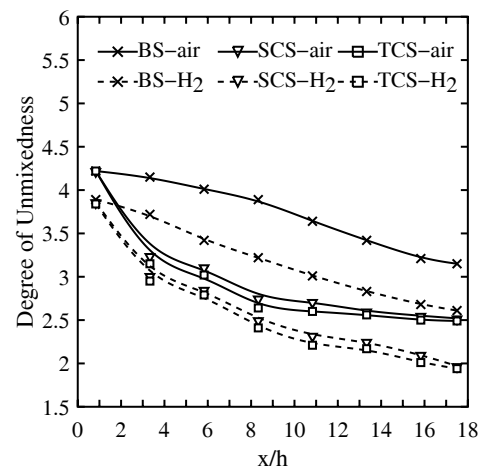for the tapered castellated strut configuration.

Figure 31. Comparison of the degree of unmixedness of
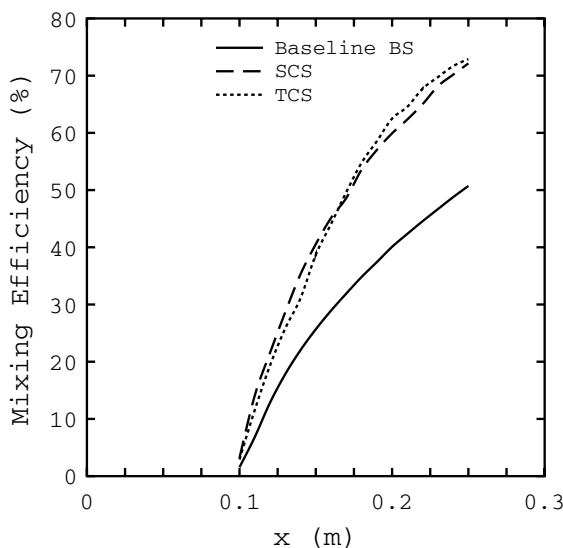air and hydrogen for different strut configurations.

Figs 9 and 12). In both the experiment and numerical results, there is not much difference between the straight and tapered castellated strut configurations. However, the discrepancy between the experimental and the predicted values may be due to a limitation in the Mie experimental imaging facility. The Mie scattering images were captured at an angle of 55 degrees from the flow direction. This was the best possible view to capture the images owing to physical constraints. Although, the experimental images were corrected for orientation, flat field and background noises, the likelihood of the presence of residual errors in the experimental images due to these factors cannot be ruled out. Whereas, the images in the numerical simulations are extracted at an angle normal to the mainstream flow and the degree of unmixedness is evaluated without the need for any corrections.

The degree of unmixedness profiles for the other strut configurations are shown in Fig. 25. As mentioned earlier, here also there is a 10% difference in the absolute values between the experimental and numerical results. However, the trends are captured well in the numerical results. The predicted decrease in the degree of unmixedness in the immediate vicinity of the strut is slightly different from the experimental results. This indicates that there is a slight under-prediction of mixing in this region. The enhancement of mixing due to vortices generated from the ramp is clearly evident by comparing the predictions near the strut base in these cases with the baseline case. Further downstream, the mixing takes place gradually. The slopes of both numerical and experimental results are almost the same beyond $X/h = 3·5$.

Figure 32. Variation of the mixing efficiency
along the length of the test section.

3.1.4 Comparison of the wall static pressure

The predicted wall static pressure along the centerline of the test section top wall is compared with experimental data[25] in Fig. 26. The wall static pressure has been non-dimensionalised using the inlet stagnation pressure. In the experiments, pressure is measured at 27 discrete axial locations along the length of the test section and with a spacing of 10mm. Figure 26 shows the wall static pressure comparison for all the six strut configurations. The flow feature near the test section inlet has been predicted better when compared to the experimental data. Flow features on the compression and expansion corners on the strut and re-attachment shocks are also captured well in the numerical simulations. It can be seen that in all the cases predictions are within 10-15 % of the experimental data except near the exit plane for a few configurations. In the baseline case, the prediction is within 5% of the experimental value along the entire length of the test section. The predictions for the tapered castellated strut configurations are equally good. However, those for the straight castellated strut configuration, are somewhat worse in the region $0\cdot2 < \times < 0\cdot3$. The predictions for the ramp configurations are also within 10% of the experimental value except near the exit where they show a considerable departure from the experimental values. Although the flow is under-expanded at the exit in both the simulations and the experiment, it is clear that the actual conditions that prevailed in the experiments near the exit plane are considerably different from what is seen in the simulations.

It is clear from the above discussion that the numerical calculations are able to predict the measured quantities well and also bring out additional insights into the mixing process. Here, air rather than an actual fuel has been used as the injectant in the same manner as the experiments. Since the castellated strut configurations show a potential for mixing enhancement, the calculations have been carried out with an actual fuel, hydrogen, for the baseline and castellated strut configurations. The results from these simulations are compared against those with air injection. The overall performance metrics are also compared between hydrogen and air injection cases.

3.2 Hydrogen injection

Figure 27 shows the comparison of the injectant (air and hydrogen) mass fraction contours at several axial locations downstream of the injector port for the baseline strut. It may be recalled that earlier, contours of mole fractions of the secondary injectant (air) were compared between the experimental and numerical results. Whereas, here, mass fraction rather than mole fraction, is used for comparison owing to the difference in mass flow rate and molecular weight between hydrogen and air injections. The spreading of hydrogen in both the spanwise and lateral directions is more pronounced when compared to air, as seen in Fig. 27.

Contours of air and hydrogen mass fractions at different axial locations are compared for the straight castellated strut in Fig. 28. Uniform mixing is seen for both hydrogen and air injection. However, at axial locations, X/h = 10·83 and 17·5, the spread of the secondary stream is seen to be different between hydrogen and air. The spread in the vertical and spanwise directions is higher in the case of hydrogen when compared to air. The lobed nature of the secondary jets in both hydrogen and air injection cases confirm the vorticity generation from the geometric modifications in the strut. The increased spreading of the injectant due to these modifications can also be seen clearly by comparing the spread pattern between Figs. 28 and 29.

Figure 29 shows the mass fraction contours of air and hydrogen for the tapered castellated strut. In the air injection case, four distinct lobes are seen at X/h = 10·83 and 17·5. Whereas, in the case of hydrogen injection, only two dominant lobes of the secondary jets are seen due to higher spreading and faster mixing rate in the vertical direction.

It is interesting to note that the spread is significantly different between the baseline and other configurations. This is due to the enhancement of mixing of the secondary injectant with the mainstream by the vortices generated from the modifications to the strut geometry. Among the castellated strut configurations, the straight castellated configuration shows a shorter core region when compared to the tapered castellated configuration. This in turn indicates that the mixing is higher in the former and this corroborates well with the results discussed earlier.

3.2.1 Degree of unmixedness

In the earlier section, the performance of different strut configurations was evaluated quantitatively using the degree of unmixedness. Similarly, here with hydrogen injection, the degree of unmixedness is used to quantify the performance of the strut configurations. This comparison will help to bring out the effect of injector configuration in conjunction with the difference in secondary injectant properties.

Figure 31 shows the performance of different strut configurations for both air and hydrogen injection. Although the trends are similar between the hydrogen and air injection, it is clearly evident from Fig. 31 that the mixing levels have increased significantly in all the configurations when hydrogen is injected. The results further show that the strut modifications augment the mixing levels when compared to the baseline case. This can be expected to result in high mixing efficiency in these strut configurations. This is discussed next.

3.2.2 Mixing efficiency

The mixing efficiency[26] is an overall performance metric that allows the effectiveness of injection strategies to be evaluated quantitatively. While the degree of unmixedness quantifies the physical spreading of the fuel, the mixing efficiency quantifies the stoichiometric mixing of the fuel. The mixing efficiency, η_m on a x = constant plane is defined as;

$$\eta_m = \frac{\int_x \alpha R \rho u\, dA}{\Sigma_x \dot{m}\, fuel, in}, \alpha R = \begin{cases} \alpha, & \alpha > \alpha_s \\ \alpha_s \dfrac{1-\alpha}{1-\alpha_s}, & \alpha > \alpha_s \end{cases}$$

where, α is the actual fuel mass fraction, αs is the stoichiometric fuel mass fraction corresponding to the oxygen mass fraction at that location, ρ is the density, u is the axial velocity and $\dot{m}$fuel,in is the mass flow rate of the fuel injected upstream of this plane. Mixing efficiency is thus a measure of the percentage of the fuel that is likely to burn under stoichiometric conditions.

Figure 32 shows the comparison of mixing efficiency between the strut configurations with hydrogen injection. The mixing efficiencies of the castellated strut (both straight and tapered) are almost 20% higher than the baseline strut configuration. This is consistent with the earlier findings. However, the performance of the straight castellated strut and tapered castellated strut are almost the same. While the maximum mixing efficiency is only 70%, it is worth noting however that the mixing increases continuously until the exit of the test section. This indicates that the test section is not long enough to achieve complete mixing. In supersonic combustors of length of the order of 1 m, the typical value of mixing efficiency for hydrogen is above 90%. The trends seen in Fig. 32 do indicate that the castellated strut designs can achieve such efficiencies if the combustor is 1 m or so in length. The results discussed above clearly establish the fact that the mixing efficiency can be significantly increased by using hyper-mixers and the proposed modifications to the baseline strut configuration are able to achieve the intended design objective of enhanced mixing.

4.0 CONCLUSIONS

In this work, numerical simulations have been carried out for six strut configurations to investigate the role of hyper-mixers on supersonic mixing. Both air as well as hydrogen has been used as injectants. A comparison of the predictions with experimentally obtained Schlieren and Mie scattering images shows that the salient flow features are captured well in the simulations. Pathlines of the secondary injectant, air, bring out the difference in the spanwise and lateral spread between the strut configurations. Modifications such as ramp and castellation to the strut are able to pull the secondary stream in the vertical direction with an increased spread in the lateral direction.

In addition to qualitative predictions, parameters such as exit stagnation pressure profile, degree of unmixedness and wall static pressure have been used to quantify the performance of different strut configurations. The predicted exit stagnation pressure agrees well with the experimental data at all the locations for the castellated strut configurations. Maximum deviation is seen near the symmetry plane for the tapered ramp at rear end strut configuration. On the other hand, predicted trends in the degree of unmixedness agree very well with the experimental trends. However, differences of about 10% in the absolute values between experiments and numerical predictions can be attributed to the difference in the manner in which the degree of unmixedness is determined. The predicted wall static pressure distribution agrees well with experimental data except in a few axial locations with a maximum difference of about 12%. The results clearly demonstrate the potential of the castellated strut configurations when compared to the other strut configurations.

Numerical simulations with hydrogen injection for the baseline and castellated strut configurations show that the spreading and mixing are higher when hydrogen is injected. This is evident from the comparison of mass fraction distribution at several axial locations and spanwise sectional plane. With hydrogen injectant also, the performance of the straight castellated and tapered castellated strut configurations are found to be superior and in comparison with the baseline strut, the mixing efficiency is found to be 20% higher.

It can be concluded that the proposed strut designs are able to increase the level of mixing for both air and hydrogen injection. In addition, in the case of hydrogen, a significant increase in the mixing efficiency and spreading is achieved when compared to the baseline strut geometry. This is due both to the higher diffusivity of hydrogen and also the modifications to the strut geometry.

The present investigation clearly demonstrates that strut based hyper-mixers are very good candidates for achieving good near field mixing in supersonic flows. It is shown that a careful design of the strut geometry in conjunction with parallel injection has been to attain a high level of mixing comparable to what can be attained with normal injection, albeit with considerably less total pressure loss.

REFERENCES

1. RAJASEKARAN, A and BABU, V. Numerical simulation of three-dimensional reacting Flow in a model supersonic combustor, *J Propulsion and Power*, 2006, **22**, (4), pp 820-827.
2. MANNA, P., BEHERA, R. and CHAKRABORTY, D. Liquid-fueled strut-based scramjet combustor design: A computational fluid dynamics approach, *J Propulsion and Power*, 2008, **24**, (2), pp 274-281
3. HSU, K.K., CARTER, C.D., GRUBER, M.R. and TAM, C.J. Mixing study of strut Injectors in supersonic flows, AIAA -2009-5226.
4. TOMIOKA, S., KOBAYASHI, K., KUDO, K., MURAKAMI, A. and KANDA, T. Performance of supersonic combustors with fuel injection in diverging section, *J Propulsion and Power*, 2006, **22**, (1), pp 111-119.
5. OWENS, M.G., SEGAL, C. and AUSLENDER, A.H. Effects of mixing schemes on kerosene combustion in a supersonic airstream, *J Propulsion and Power*, 1997, **13**, (4), pp 525-531.
6. KARAGOZIAN, A.R., WANG, K.C., LE, A.T. and SMITH, O.I. Transverse gas injection behind a rearward-facing step, *J Propulsion and Power*, 1996, **12**, (6), pp 1129-1136.
7. BEN-YAKAR, A. and HANSON, R.K. Cavity flame-holders for ignition and flame stabilisation in scramjets: An overview, *J Propulsion and Power*, 2001, **17**, (4), pp 869-877.
8. GRUBER, M.R., BAURLE, R.A., MATHUR, T. and HSU, K.Y. Fundamental studies of cavity-based flameholder concepts for supersonic combustors, *J Propulsion and Power*, 2001, **17**, (1), pp 146-153.
9. GRUBER, M.R., DONBAR, J.M., CARTER, C.D. and HSU, K.Y. Mixing and combustion studies using cavity-based flameholders in a supersonic flow, *J Propulsion and Power*, 2004, **20**, (5), pp 769-778.
10. DONOHUE, J.M., McDANIEL, J.C. and HAJ-HARIRI, H. Experimental and numerical study of swept ramp injection into a supersonic flow field, *AIAA J*, 1994, **32**, (9), pp 1860–1867.
11. FULLER R.P., WU, P.K., NEJAD, A.S. and SCHETZ, J.A. Comparison of physical and aerodynamic ramps as fuel injectors in supersonic flow, *J Propulsion and Power*, 1998, **14**, (2), pp 135-145.
12. WILSON M.P., BOWERSOX, R.D.W. and GLAWE, D.D. Experimental investigation of the role of downstream ramps on a supersonic injection plume, *J Propulsion and Power*, 1999, **15**, (3), pp 432-439.
13. BOGDANOFF D.W. Advanced injection and mixing techniques for scramjet combustors, *J Propulsion and Power*, 1994, **10**, (2), pp 183-190.
14. GRUENIG C., AVRASHKOV, V. and MAYINGER, F. Fuel injection into a supersonic airflow by means of pylons, *J Propulsion and Power*, 2000, **16**, (1), pp 29-34.
15. TEW, D.E., WAITZ, I.A. and HERMANSON, J.C. Streamwise vorticity enhanced mixing downstream of lobed mixers, AIAA-95-2746, 1995.
16. SUNAMI, T., WENDT, M.N. and NISHIOKA, M. Supersonic mixing and combustion control using streamwise vortices, AIAA-1998-3271, 1998
17. KODERA, M., SUNAMI, T. and SHEEL, F. Numerical study on the supersonic mixing enhancement using streamwise vortices, AIAA-2002-5117, 2002
18. CLEMENS, N.T. and MUNGAL, M.G. Two and three dimensional effects in the supersonic mixing layers, *AIAA J*, 1992, **20**, (4), pp 973-981.
19. PAPAMOSCHOU, D. Effect of three dimensionality on compressible mixing layers, *J Propulsion and Power*, 1992, **8**, (1), pp 247-249.
20. DESIKAN, S.L.N. and KURIAN, J. Strut-based gaseous injection into a supersonic stream, *J Propulsion and Power*, 2006, **22**, (2), pp 474-477.
21. MENTER, F.R. Zonal two equation k-ω models for aerodynamic flows, AIAA-93-2906, 1993.
22. BRADSHAW, P., FERRISS, D.H. and ATWELL, N.P. Calculation of boundary-layer development using the turbulent energy equation, *J Fluid Mechanics*, 1967, **28**, (3), pp 593-616.
23. BAURLE, R.A. and EKLUND, D.R. Analysis of dual-mode hydrocarbon scramjet operation at Mach 4-6.5, *J Propulsion and Power*, 2002, **18**, (5), pp 990-1002.
24. RAJASEKARAN, A. and BABU, V. On the effect of Schmidt and Prandtl numbers in the numerical predictions of supersonic combustion, AIAA paper 06-5037, 2006.
25. DESIKAN, S.L.N. and KURIAN, J. Mixing studies in supersonic flow employing strut based hypermixers, AIAA Paper 2005-3643, 2005.
26. BAURLE, R.A., MATHUR, T., GRUBER, M.R. and JACKSON, K.R.A Numerical and experimental investigation of a scramjet combustor for hypersonic missile applications, AIAA Paper 98-3121, 1998.